Maximal spontaneous photon emission and energy loss from free electrons

Yi Yang [1]*, Aviram Massuda[1], Charles Roques-Carmes [1], Steven E. Kooi [2], Thomas Christensen[1], Steven G. Johnson[1], John D. Joannopoulos[1,2], Owen D. Miller [3]*, Ido Kaminer [1,4]* and Marin Soljačić[1]

Free-electron radiation such as Cerenkov[1], Smith–Purcell[2] and transition radiation[3,4] can be greatly affected by structured optical environments, as has been demonstrated in a variety of polaritonic[5,6], photonic-crystal[7] and metamaterial[8–10] systems. However, the amount of radiation that can ultimately be extracted from free electrons near an arbitrary material structure has remained elusive. Here we derive a fundamental upper limit to the spontaneous photon emission and energy loss of free electrons, regardless of geometry, which illuminates the effects of material properties and electron velocities. We obtain experimental evidence for our theory with quantitative measurements of Smith–Purcell radiation. Our framework allows us to make two predictions. One is a new regime of radiation operation—at subwavelength separations, slower (non-relativistic) electrons can achieve stronger radiation than fast (relativistic) electrons. The other is a divergence of the emission probability in the limit of lossless materials. We further reveal that such divergences can be approached by coupling free electrons to photonic bound states in the continuum[11–13]. Our findings suggest that compact and efficient free-electron radiation sources from microwaves to the soft X-ray regime may be achievable without requiring ultrahigh accelerating voltages.

The Smith–Purcell effect epitomizes the potential of free-electron radiation. Consider an electron at velocity $\beta = v/c$ traversing a structure with periodicity a; it generates far-field radiation at wavelength λ and polar angle θ, dictated by[2]

$$\lambda = \frac{a}{m}\left(\frac{1}{\beta} - \cos\theta\right) \tag{1}$$

where m is the integer diffraction order. The absence of a minimum velocity in equation (1) offers prospects for threshold-free and spectrally tunable light sources, spanning from microwave and terahertz[14–16], across visible[17–19], and towards X-ray[20] frequencies. In stark contrast to the simple momentum-conservation determination of wavelength and angle, there is no unified yet simple analytical equation for the radiation intensity. Previous theories offer explicit solutions only under strong assumptions (for example, assuming perfect conductors or employing effective medium descriptions) or for simple, symmetric geometries[21–23]. Consequently, heavily numerical strategies are often an unavoidable resort[24,25]. In general, the inherent complexity of the interactions between electrons and photonic media have prevented a more general understanding of how pronounced spontaneous electron radiation can ultimately be for arbitrary structures, and consequently, how to design the maximum enhancement for free-electron light-emitting devices.

We begin our analysis by considering an electron (charge $-e$) of constant velocity $v\hat{x}$ traversing a generic scatterer (plasmonic or dielectric, finite or extended) of arbitrary size and material composition, as in Fig. 1a. The free current density of the electron, $\mathbf{J}(\mathbf{r}, t) = -\hat{\mathbf{x}}ev\delta(y)\delta(z)\delta(x - vt)$, generates a frequency-dependent ($e^{-i\omega t}$ convention) incident field[26]

$$\mathbf{E}_{\text{inc}}(\mathbf{r}, \omega) = \frac{e\kappa_\rho e^{ik_\nu x}}{2\pi\omega\varepsilon_0}[\hat{\mathbf{x}}i\kappa_\rho K_0(\kappa_\rho\rho) - \hat{\boldsymbol{\rho}}k_\nu K_1(\kappa_\rho\rho)] \tag{2}$$

written in cylindrical coordinates (x, ρ, ψ); here, K_n is the modified Bessel function of the second kind, $k_\nu = \omega/v$ and $\kappa_\rho = \sqrt{k_\nu^2 - k^2} = k/\beta\gamma$ ($k = \omega/c$, free-space wavevector; $\gamma = 1/\sqrt{1 - \beta^2}$, Lorentz factor). Hence, the photon emission and energy loss of free electrons can be treated as a scattering problem: the electromagnetic fields $\mathbf{F}_{\text{inc}} = (\mathbf{E}_{\text{inc}}, Z_0\mathbf{H}_{\text{inc}})^{\text{T}}$ (for free-space impedance Z_0) are incident on a photonic medium with material susceptibility $\overline{\overline{\chi}}$ (a 6×6 tensor for a general medium), causing both absorption and far-field scattering—that is, photon emission—that together comprise electron energy loss (Fig. 1a).

As recently shown in refs [27–29], for a generic electromagnetic scattering problem, passivity—the condition that polarization currents do no net work—constrains the maximum optical response from a given incident field. Consider three power quantities derived from $\mathbf{F}_{\text{inc}}$ and the total field $\mathbf{F}$ within the scatterer volume V: the total power lost by the electron, $P_{\text{loss}} = -(1/2)\text{Re}\int_V \mathbf{J}^\star \cdot \mathbf{E}\,\mathrm{d}V = (\epsilon_0\omega/2)\text{Im}\int_V \mathbf{F}_{\text{inc}}^\dagger \overline{\overline{\chi}}\mathbf{F}\,\mathrm{d}V$, the power absorbed by the medium, $P_{\text{abs}} = (\epsilon_0\omega/2)\text{Im}\int_V \mathbf{F}^\dagger \overline{\overline{\chi}}\mathbf{F}\,\mathrm{d}V$, and their difference, the power radiated to the far field, $P_{\text{rad}} = P_{\text{loss}} - P_{\text{abs}}$. Treating $\mathbf{F}$ as an independent variable, the total loss P_{loss} is a linear function of $\mathbf{F}$, whereas the fraction that is dissipated is a quadratic function of $\mathbf{F}$. Passivity requires non-negative radiated power, represented by the inequality $P_{\text{abs}} < P_{\text{loss}}$, which in this framework is therefore a convex constraint on any response function. Constrained maximization (see Supplementary Section 1) of the energy-loss and photon-emission power quantities, P_{loss} and P_{rad}, directly yields the limits

$$P_\tau(\omega) \leq \frac{\varepsilon_0\omega\xi_\tau}{2}\int_V \mathbf{F}_{\text{inc}}^\dagger \overline{\overline{\chi}}^\dagger(\text{Im}\overline{\overline{\chi}})^{-1}\overline{\overline{\chi}}\,\mathbf{F}_{\text{inc}}\,\mathrm{d}V \tag{3}$$

[1]Research Laboratory of Electronics, Massachusetts Institute of Technology, Cambridge, MA, USA. [2]Institute for Soldier Nanotechnologies, Cambridge, MA, USA. [3]Department of Applied Physics and Energy Sciences Institute, Yale University, New Haven, CT, USA. [4]Andrew and Erna Viterbi Department of Electrical Engineering, Technion-Israel Institute of Technology, Haifa, Israel. *e-mail: yiy@mit.edu; owen.miller@yale.edu; kaminer@technion.ac.il
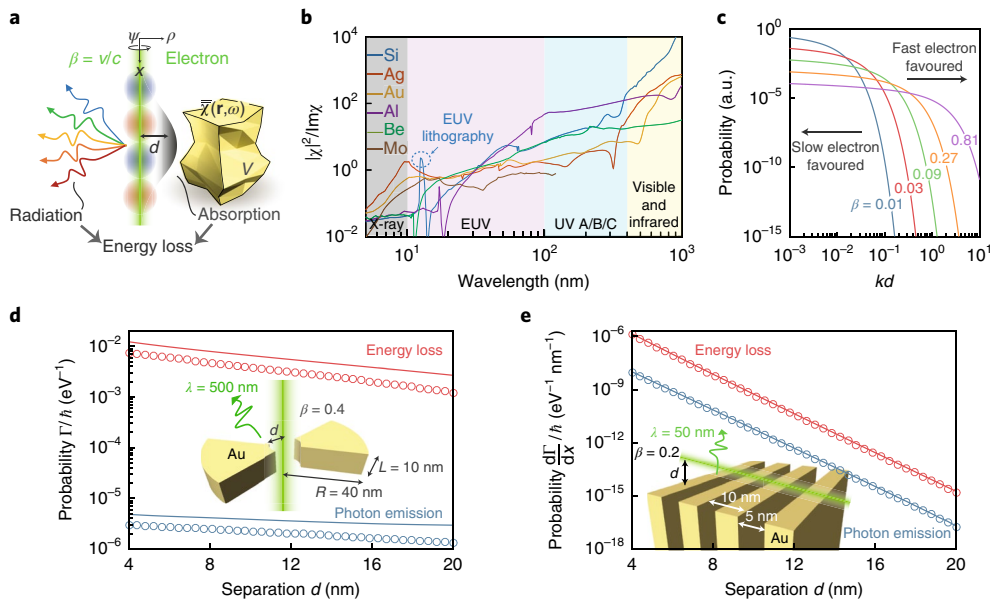
Fig. 1 | Theoretical framework and predictions. a, The interaction between a free electron and an obstacle defined by a susceptibility tensor $(\mathbf{r}, \omega)$ within a volume V, located at a distance d, generates electron energy loss into radiation and absorption. **b**, $|\chi|^2/\mathrm{Im}\chi$ constrains the maximum material response to the optical excitations of free electrons over different spectral ranges for representative materials (from ref. [40]). At the X-ray and extreme ultraviolet (EUV) regime, Si is optimal near the technologically relevant 13.5 nm (dashed circle). Contrary to the image charge intuition for the optical excitations of electrons, low-loss dielectrics (such as Si in the visible and infrared regimes) can be superior to metals. **c**, Shape-independent upper limit showing superiority of slow or fast electrons at small or large separations; the material affects only the overall scaling. **d**,**e**, Numerical simulations (circles) compared to analytical upper limits (lines; equation (5a) for **d** and equation (6) for **e**, respectively) for the radiation (blue) and energy loss (red) of electrons penetrating the centre of an annular bowtie antenna (**d**) and passing above a grating (**e**).

where $\tau \in \{\mathrm{rad}, \mathrm{loss}\}$ and ξ_τ accounts for a variable radiative efficiency η (defined as the ratio of radiative to total energy loss): $\xi_{\mathrm{loss}} = 1$ and $\xi_{\mathrm{rad}} = \eta(1-\eta) \leq 1/4$. Hereafter, we consider isotropic and non-magnetic materials (and thus a scalar susceptibility χ), but the generalizations to anisotropic and/or magnetic media are straightforward.

Combining equations (2) and (3) yields a general limit on the loss or emission spectral probabilities $\Gamma_\tau(\omega) = P_\tau(\omega)/\hbar\omega$:

$$\Gamma_\tau(\omega) \leq \frac{\alpha \xi_\tau c}{2\pi\omega^2} \int_V \frac{|\chi|^2}{\mathrm{Im}\chi} [\kappa_\rho^4 K_0^2(\kappa_\rho\rho) + \kappa_\rho^2 k_v^2 K_1^2(\kappa_\rho\rho)] \, \mathrm{d}V \qquad (4)$$

where α is the fine-structure constant. Equation (4) imposes, without solving Maxwell's equations, a maximum rate of photon generation based on the electron velocity β (through k_v and κ_ρ), the material composition $\chi(\mathbf{r})$ and the volume V.

The limit in equation (4) can be further simplified by removing the shape dependence of V, since the integrand is positive and is thus bounded above by the same integral for any enclosing structure. A scatterer separated from the electron by a minimum distance d can be enclosed within a larger concentric hollow cylinder sector of inner radius d and outer radius ∞. For such a sector (height L and opening azimuthal angle $\psi \in (0, 2\pi)$), equation (4) can be further simplified, leading to a general closed-form shape-independent limit (see Supplementary Section 2) that highlights the pivotal role of the impact parameter $\kappa_\rho d$:

$$\Gamma_\tau(\omega) \leq \frac{\alpha \xi_\tau}{2\pi c} \frac{|\chi|^2}{\mathrm{Im}\chi} \frac{L\psi}{\beta^2} [(\kappa_\rho d) K_0(\kappa_\rho d) K_1(\kappa_\rho d)] \qquad (5a)$$

$$\propto \frac{1}{\beta^2} \begin{cases} \ln(1/\kappa_\rho d) & \text{for } \kappa_\rho d \ll 1, \\ \pi e^{-2\kappa_\rho d}/2 & \text{for } \kappa_\rho d \gg 1 \end{cases} \qquad (5b)$$

The limits of equations (4), (5a) and (5b) are completely general; they set the maximum photon emission and energy loss of an electron beam coupled to an arbitrary photonic environment in either the non-retarded or retarded regimes, given only the beam properties and material composition. The key factors that determine maximal radiation are identified: intrinsic material loss (represented by $\mathrm{Im}\chi$), electron velocity β and impact parameter $\kappa_\rho d$. The metric $|\chi|^2/\mathrm{Im}\chi$ reflects the influence of the material choice, which depends sensitively on the radiation wavelength (Fig. 1b). The electron velocity β also appears implicitly in the impact parameter $\kappa_\rho d = kd/\beta\gamma$, showing that the relevant length scale is set by the relativistic velocity of the electron. The impact parameter $\kappa_\rho d$ reflects the influence of the Lorentz contraction d/γ; a well-known feature of both electron radiation and acceleration[20,26,30].

A surprising feature of the limits in equations (4), (5a) and (5b) is their prediction for optimal electron velocities. As shown in Fig. 1c, when electrons are in the far field of the structure ($\kappa_\rho d \gg 1$), stronger photon emission and energy loss are achieved by faster electrons—a well-known result. On the contrary, if electrons are in the near field ($\kappa_\rho d \ll 1$), slower electrons are optimal. This contrasting behaviour is evident in the asymptotics of equation (5b), where the $1/\beta^2$ or $e^{-2\kappa_\rho d}$ dependence is dominant at short or large separations. Physically, the optimal velocities are determined by the incident-field properties (equation (2)): slow electrons generate stronger near-field amplitudes although they are more evanescent (Supplementary Section 2). There has been recent interest in using low-energy electrons for Cherenkov[10] and Smith–Purcell[31] radiation; our prediction that they can be optimal at subwavelength interaction distances underscores the substantial technological potential of non-relativistic free-electron radiation sources.

The tightness of the limit (equations (4), (5a) and (5b)) is demonstrated by comparison with full-wave numerical calculations

(see Methods) in Fig. 1d,e. Two scenarios are considered: in Fig. 1d, an electron traverses the centre of an annular Au bowtie antenna and undergoes antenna-enabled transition radiation ($\eta \approx 0.07\%$), while, in Fig. 1e, an electron traverses a Au grating, undergoing Smith–Purcell radiation ($\eta \approx 0.9\%$). In both cases, the numerical results closely trail the upper limit at the considered wavelengths, showing that the limits can be approached or even attained with modest effort.

Next, we specialize in the canonical Smith–Purcell set-up illustrated in Fig. 1e inset. This set-up warrants a particularly close study, given its prominent historical and practical role in free-electron radiation. Aside from the shape-independent limit (equations (5a) and (5b)), we can find a sharper limit (in per unit length for periodic structure) specifically for Smith–Purcell radiation using rectangular gratings of filling factor Λ (see Supplementary Section 3)

$$\frac{d\Gamma_\tau(\omega)}{dx} \leq \frac{\alpha \xi_\tau}{2\pi c} \frac{|\chi|^2}{\text{Im}\chi} \Lambda \mathcal{G}(\beta, kd) \qquad (6)$$

The function $\mathcal{G}(\beta, kd)$ is an azimuthal integral (see Supplementary Section 3) over the Meijer G-function $G_{1,3}^{3,0}$ (ref. [32]) that arises in the radial integration of the modified Bessel functions K_n. We emphasize that equation (6) is a specific case of equation (4) for grating structures without any approximations and thus can be readily generalized to multi-material scenarios (see Supplementary equation (37)).

The grating limit (equation (6)) exhibits the same asymptotics as equations (5a) and (5b), thereby reinforcing the optimal-velocity predictions of Fig. 1c. The (β, kd) dependence of $\mathcal{G}$ (see Fig. 2a) shows that slow (fast) electrons maximize Smith–Purcell radiation in the small (large) separation regime. We verify the limit predictions by comparison with numerical simulations: at small separations (Fig. 2b), radiation and energy loss peak at velocity $\beta \approx 0.15$, consistent with the limit maximum; at large separations (Fig. 2c), both the limit and the numerical results grow monotonically with β.

The derived upper limit also applies to Cherenkov and transition radiation, as well as bulk loss in electron energy-loss spectroscopy. For these scenarios where electrons enter material bulk, a subtlety arises for the field divergence along the electron's trajectory ($\rho = 0$ in equation (2)) within a potentially lossy medium. This divergence, however, can be regularized by introducing natural, system-specific momentum cutoffs[26], which then directly permits the application of our theory (see Supplementary Section 6). Meanwhile, there exist additional competing interaction processes (for example, electrons colliding with individual atoms). However, they typically occur at much smaller length scales.

We perform quantitative experimental measurement of Smith–Purcell radiation to directly probe the upper limit. Figure 3a shows our experimental set-up (see Methods and Supplementary Section 7 for details). A one-dimensional (1D) 50%-filling-factor grating (Au-covered single-crystalline Si)—the quintessential Smith–Purcell set-up—is chosen as a sample, and shown by scanning electron microscope (SEM) images in Fig. 3b,c. Free electrons pass above and impinge onto the sample at a grazing angle of 1.5° under 10 to 20 kV acceleration voltages.

Figure 3d depicts our measurements of first-order $m = 1$ Smith–Purcell radiation appearing at wavelengths between 500 and 750 nm. In quantitative agreement with equation (1) evaluated at the normal emission angle (solid lines), the measured radiation spectra (dots) blueshift with increasing electron velocity. Notably, we experimentally obtain the absolute intensity of the collected radiation via a calibration measurement (see Supplementary Section 7). The upper limits (equation (4)) for the surface-normal emission wavelengths ($\lambda = a/\beta$) are evaluated at the centre of the interaction region (height ≈ 140 nm ($kd \approx 1.5$), varying with beam energy), and is shown with shading in Fig. 3d to account for the thickness uncertainty
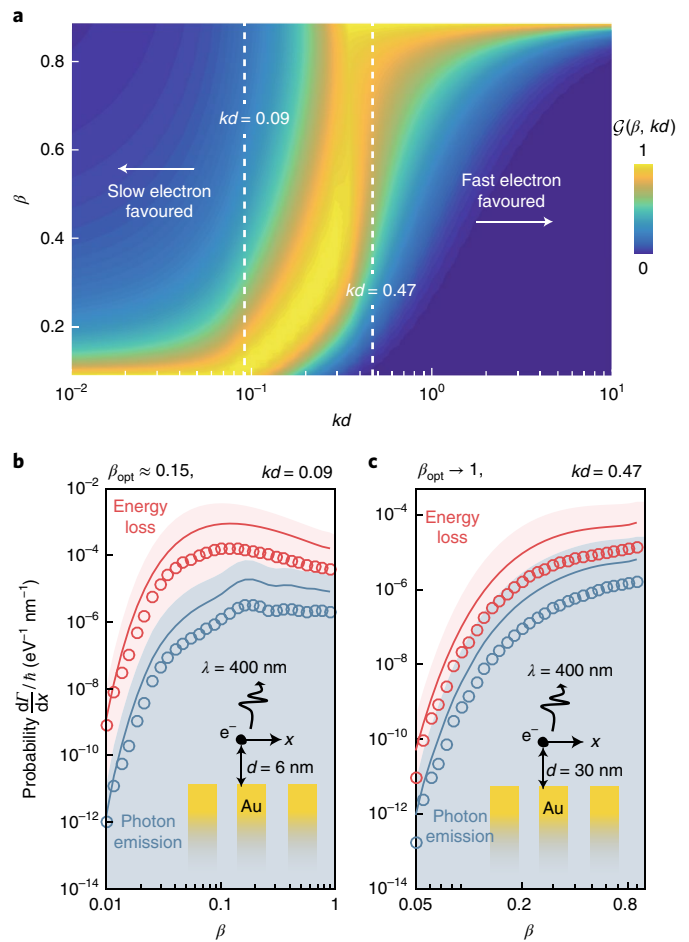
Fig. 2 | Optimal electron velocities for maximal Smith–Purcell radiation. **a**, Behaviour of $\mathcal{G}(\beta, kd)$, equation (6), whose maxima indicate separation-dependent optimal electron velocities. Here $\mathcal{G}$ is normalized between 0 and 1 for each separation. The limit yields sharply contrasting predictions: slow electrons are optimal in the near field ($kd \ll 1$) and fast electrons are optimal in the far field ($kd \gg 1$). **b,c**, Energy loss (red) and radiation (blue) rates (circles: full-wave simulations; lines: grating limit, equation (6); shading: shape-independent limit, equations (5a) and (5b)) at two representative near/far-field separation distances (white dashed slices in **a**).

(± 1.5 nm). The envelope spanned by the measurement peaks follows the upper-limit lineshape across the visible spectrum: both the theoretical limit and the measured intensities peak near 550 nm and decrease in a commensurate manner for other wavelengths. This lineshape originates from two competing factors. At shorter wavelengths, the material factor $|\chi|^2/\text{Im}\chi$ decreases significantly for both Au and Si (see Fig. 1c), which accounts for the reduced radiation intensity. At longer wavelengths, the major constraint becomes the less efficient interaction between the electrons and the structure, as the electron-beam diameters increase for the reduced brightness of the electron gun (tungsten) at lower acceleration voltages (see Supplementary Section 7). These pieces of experimental evidence for the upper limit are at $kd \approx 1.5$ (estimated from a geometrical ray-tracing model; see Supplementary Section 7), where fast electrons are still preferred (Fig. 2a). To further confirm our theory, we also conduct a near-infrared Smith–Purcell experiment (Supplementary Section 8) at $kd \approx 1$, where the envelope lineshape of the emission spectra again follows our prediction. We also obtain complementary supporting evidence (extracted from a recent work[10]) for our slow-electron-efficient prediction (see Supplementary Section 9).
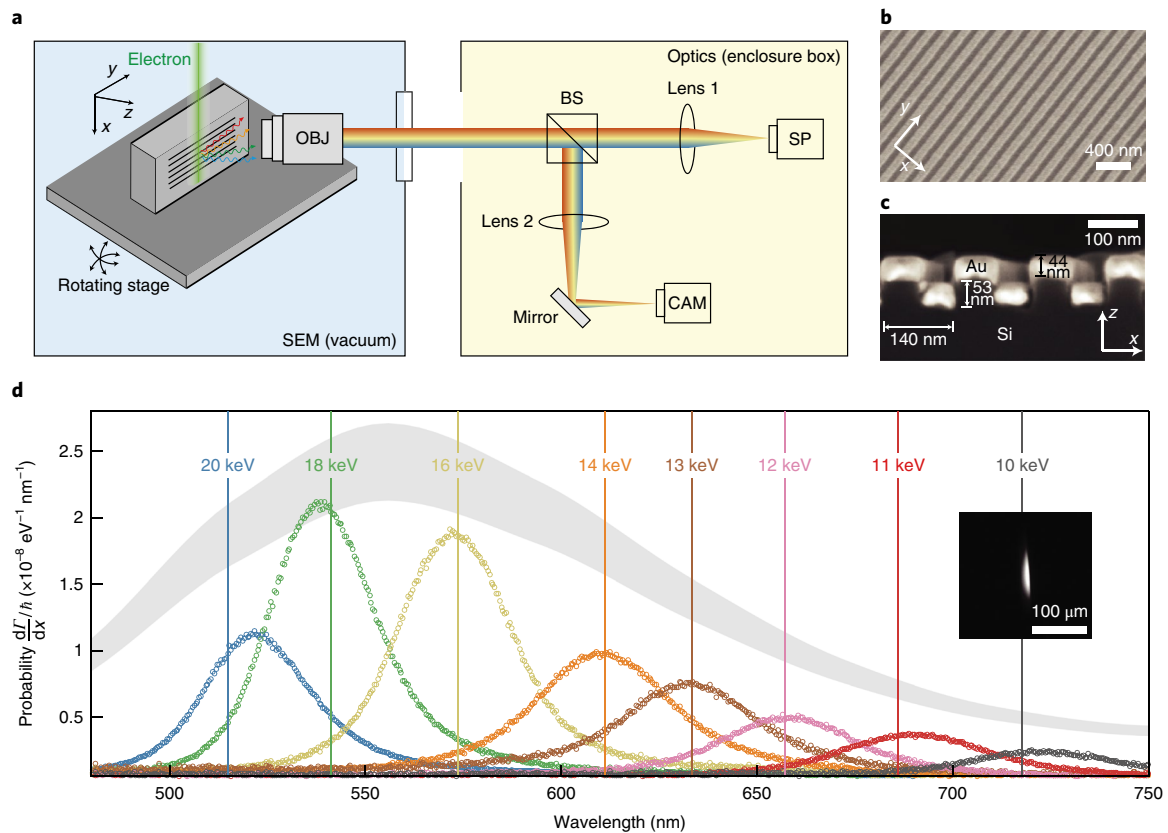
Fig. 3 | Experimental probing of the upper limit. a, Experimental set-up. OBJ, objective (numerical aperture of 0.3); BS, beamsplitter; SP, spectrometer; CAM, camera. **b,c**, SEM images of the structure in top view (**b**) and cross-sectional view (**c**). **d**, Quantitative measurement of Smith–Purcell radiation (inset: camera image of the radiation). The solid lines mark the theoretical radiation wavelengths at the normal angle (equation (1)). The envelope (peak outline) of the measured spectra (dots) follows the theoretical upper limit (shaded to account for fabrication tolerance; calculated at each wavelength with the corresponding electron velocity for surface-normal radiation).

Finally, we turn our attention to an ostensible peculiarity of the limits: equation (4) evidently diverges for lossless materials (Im$\chi \to 0$), seemingly providing little insight. On the contrary, this divergence suggests the existence of a mechanism capable of strongly enhancing Smith–Purcell radiation. Indeed, by exploiting high-Q resonances near bound states in the continuum (BICs)[13] in photonic crystal slabs, we find that Smith–Purcell radiation can be enhanced by orders of magnitude, when specific frequency-, phase- and polarization-matching conditions are met.

A 1D silicon ($\chi = 11.25$)-on-insulator (SiO$_2$, $\chi = 1.07$) grating interacting with a sheet electron beam illustrates the core conceptual idea most clearly. The transverse electric (TE) (E_x, H_y, E_z) band structure (lowest two bands labelled TE$_0$ and TE$_1$), matched polarization for a sheet electron beam (supplementary equation S41b)), is depicted in Fig. 4b along the $\Gamma-X$ direction. Folded electron wavevectors, $k_v = \omega/v$, are overlaid for two distinct velocities (blue and green). Strong electron–photon interactions are possible when the electron and photon dispersions intersect: for instance, k_v and the TE$_0$ band intersect (grey circles) below the air light cone (light yellow shading). However, these intersections are largely impractical: the TE$_0$ band is evanescent in the air region, precluding free-space radiation. Still, analogous ideas, employing similar partially guided modes, such as spoof plasmons[33], have been explored for generating electron-enabled guided waves[34,35].

To overcome this deficiency, we theoretically propose a new mechanism for enhanced Smith–Purcell radiation: coupling of electrons with BICs[13]. The latter have the extreme quality factors of guided modes but are, crucially, embedded in the radiation continuum, guaranteeing any resulting Smith–Purcell radiation into the far field. By choosing appropriate velocities $\beta = a/m\lambda$ (m being any integer; λ being the BIC wavelength) such that the electron line (blue or green) intersects the TE$_1$ mode at the BIC (red square in Fig. 4b), the strong enhancements of a guided mode can be achieved in tandem with the radiative coupling of a continuum resonance. In Fig. 4c, the incident fields of electrons and the field profile of the BIC indicate their large modal overlaps. The BIC field profile shows complete confinement without radiation, unlike conventional multipolar radiation modes (see Supplementary Fig. 9). The Q values of the resonances are also provided near a symmetry-protected BIC[13] at the Γ point. Figure 4d,e demonstrates the velocity tunability of BIC-enhanced radiation—as the phase matching approaches the BIC, a divergent radiation rate is achieved.

The BIC-enhancement mechanism is entirely accordant with our upper limits. Practically, silicon has non-zero loss across the visible and near-infrared wavelengths. For example, for a period of $a = 676$ nm, the optimally enhanced radiation wavelength is $\approx 1,050$ nm, at which $\chi_{Si} \approx 11.25 + 0.001i$ (ref. [36]). For an electron–structure separation of 300 nm, we theoretically show in Fig. 4f the strong radiation enhancements (>3 orders of magnitude) attainable by BIC-enhanced coupling. The upper limit (shaded region; 2D analogue of equation (4); see Supplementary Section 10) attains extremely large values due to the minute material loss ($|\chi|^2/\text{Im}\chi \approx 10^5$); nevertheless, BIC-enhanced coupling enables the radiation intensity to closely approach this limit at several resonant velocities. In the presence of an absorptive channel, the maximum enhancement occurs at a small offset from the BIC where the Q-matching condition (see Supplementary Section 11) is satisfied (that is, equal absorptive and radiative rates of the resonances).
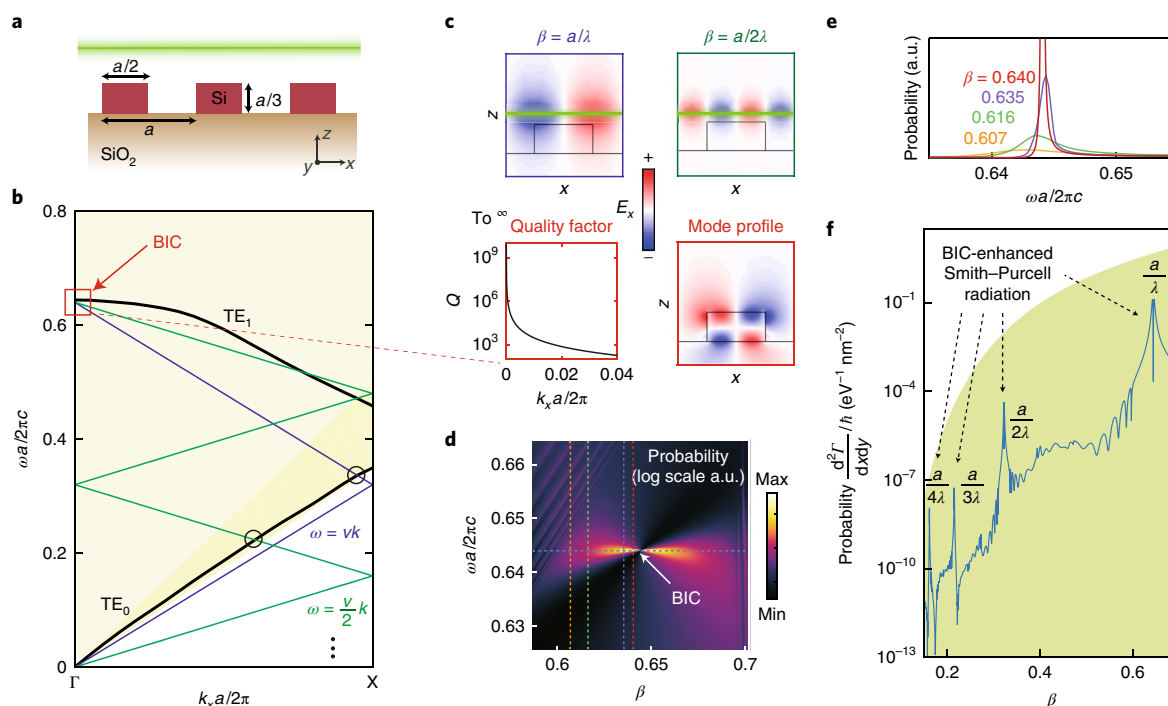
Fig. 4 | Strong enhancement of Smith–Purcell radiation via high-Q resonances near a photonic BIC. a, A schematic drawing of a silicon-on-insulator grating (1D photonic crystal slab: periodic in x and infinite in y). **b**, The calculated TE band structure (solid black lines) in the $\Gamma-X$ direction. The area shaded in light and dark yellow indicates the light cone of air and silica, respectively. The electron lines (blue for velocity v, and green for $v/2$) can phase match with either the guided modes (circles) or high-Q resonances near a BIC (red square). **c**, Upper: incident field of electrons. Lower: resonant quality factors (left) and eigenmode profile (right) near a BIC. **d**, Strongly enhanced Smith–Purcell radiation near the BIC. **e**, Vertical slices of **d**. **f**, The limit (shaded area) compared with the horizontal slice of **d**, with material loss considered. Strong enhancement happens at electron velocities $\beta = a/m\lambda$ ($m = 1, 2, 3 \ldots$).

In closing, we have theoretically derived and experimentally probed a universal upper limit to the energy loss and photon emission from free electrons. The limit depends crucially on the impact parameter $\kappa_\rho d$, but not on any other detail of the geometry. Hence, our limit applies even to the most complex metamaterials and metasurfaces, given only their constituents. Surprisingly, in the near field, slow electrons promise stronger radiation than relativistic ones. The limit predicts a divergent radiation rate as the material loss rate goes to zero, and we show that BIC resonances enable such staggering enhancements. This is relevant for the generation of coherent Smith–Purcell radiation[14,34,35]. The long lifetime, spectral selectivity and large field enhancement near a BIC can strongly bunch electrons, allowing them to radiate coherently at the same desired frequency, potentially enabling low-threshold Smith–Purcell free-electron lasers. The combination of this mechanism and the optimal velocity prediction reveals prospects of low-voltage yet high-power free-electron radiation sources. In addition, our findings demonstrate a simple guiding principle to maximize the signal-to-noise ratio for electron energy-loss spectroscopy through an optimal choice of electron velocity, enabling improved spectral resolution.

The predicted slow-electron-efficient regime still calls for direct experimental validation. We suggest that field-emitter-integrated free-electron devices (for example, ref. [10]) are ideal to confirm the prediction due to the achievable small electron–structure separation and high electron beam quality at relatively large currents. Alternatively, the microwave or terahertz frequencies could be suitable spectral ranges for verifying the slow-electron-efficient regime, where the subwavelength separation requirement is more achievable.

The upper limit demonstrated here is in the spontaneous emission regime for constant-velocity electrons, and can be extended to the stimulated regime by suitable reformulation. Stronger electron–photon interactions can change electron velocity by a non-negligible amount that alters the radiation. If necessary, this correction can be perturbatively incorporated. In the case of external optical pumping[37], the upper limit can be revised by redefining the incident field as the summation of the electron incident field and the external optical field. From a quantum mechanical perspective, this treatment corresponds to stimulated emission from free electrons, which multiplies the limit by the number of photons in that radiation mode. This treatment could also potentially translate our limit into a fundamental limit for particle acceleration[38,39], which is the time-reversal of free-electron energy loss and which typically incorporates intense laser pumping. In the multi-electron scenario, the radiation upper limit will be obtained in the case of perfect bunching, where all electrons radiate in phase. In this case, our single-electron limit should be multiplied by the number of electrons to correct for the superradiant nature of such coherent radiation.

Methods

Methods, including statements of data availability and any associated accession codes and references, are available at https://doi.org/10.1038/s41567-018-0180-2

References

1. Cherenkov, P. A. Visible glow under exposure of gamma radiation. *Dokl. Akad. Nauk SSSR* **2**, 451–454 (1934).

2. Smith, S. J. & Purcell, E. Visible light from localized surface charges moving across a grating. *Phys. Rev.* **92**, 1069 (1953).
3. Ginsburg, V. & Frank, I. Radiation of a uniformly moving electron due to its transition from one medium into another. *Zh. Eksp. Teor. Fiz.* **16**, 15–28 (1946).
4. Goldsmith, P. & Jelley, J. Optical transition radiation from protons entering metal surfaces. *Philos. Mag.* **4**, 836–844 (1959).
5. Liu, S. et al. Surface polariton Cherenkov light radiation source. *Phys. Rev. Lett.* **109**, 153902 (2012).
6. Kaminer, I. et al. Efficient plasmonic emission by the quantum Čerenkov effect from hot carriers in graphene. *Nat. Commun.* **7**, ncomms11880 (2016).
7. Luo, C., Ibanescu, M., Johnson, S. G. & Joannopoulos, J. Cerenkov radiation in photonic crystals. *Science* **299**, 368–371 (2003).
8. Adamo, G. et al. Light well: a tunable free-electron light source on a chip. *Phys. Rev. Lett.* **103**, 113901 (2009).
9. Ginis, V., Danckaert, J., Veretennicoff, I. & Tassin, P. Controlling Cherenkov radiation with transformation-optical metamaterials. *Phys. Rev. Lett.* **113**, 167402 (2014).
10. Liu, F. et al. Integrated Cherenkov radiation emitter eliminating the electron velocity threshold. *Nat. Photon.* **11**, 289–292 (2017).
11. Hsu, C. W. et al. Observation of trapped light within the radiation continuum. *Nature* **499**, 188–191, (2013).
12. Yang, Y., Peng, C., Liang, Y., Li, Z. & Noda, S. Analytical perspective for bound states in the continuum in photonic crystal slabs. *Phys. Rev. Lett.* **113**, 037401 (2014).
13. Hsu, C. W., Zhen, B., Stone, A. D., Joannopoulos, J. D. & Soljacic, M. Bound states in the continuum. *Nat. Rev. Mater.* **1**, 16048 (2016).
14. Urata, J. et al. Superradiant Smith–Purcell emission. *Phys. Rev. Lett.* **80**, 516–519 (1998).
15. Korbly, S., Kesar, A., Sirigiri, J. & Temkin, R. Observation of frequency-locked coherent terahertz Smith-Purcell radiation. *Phys. Rev. Lett.* **94**, 054803 (2005).
16. Doucas, G., Mulvey, J., Omori, M., Walsh, J. & Kimmitt, M. First observation of Smith-Purcell radiation from relativistic electrons. *Phys. Rev. Lett.* **69**, 1761–1764 (1992).
17. Kube, G. et al. Observation of optical Smith-Purcell radiation at an electron beam energy of 855 MeV. *Phys. Rev. E* **65**, 056501 (2002).
18. Yamamoto, N., de Abajo, F. J. G. & Myroshnychenko, V. Interference of surface plasmons and Smith-Purcell emission probed by angle-resolved cathodoluminescence spectroscopy. *Phys. Rev. B* **91**, 125144 (2015).
19. Kaminer, I. et al. Spectrally and spatially resolved Smith-Purcell radiation in plasmonic crystals with short-range disorder. *Phys. Rev. X* **7**, 011003 (2017).
20. Moran, M. J. X-ray generation by the Smith-Purcell effect. *Phys. Rev. Lett.* **69**, 2523–2526 (1992).
21. van den Berg, P. Smith-Purcell radiation from a point charge moving parallel to a reflection grating. *J. Opt. Soc. Am.* **63**, 1588–1597 (1973).
22. Haeberlé, O., Rullhusen, P., Salomé, J.-M. & Maene, N. Calculations of Smith-Purcell radiation generated by electrons of 1–100 MeV. *Phys. Rev. E* **49**, 3340–3352 (1994).
23. Sergeeva, D. Y., Tishchenko, A. & Strikhanov, M. Conical diffraction effect in optical and x-ray Smith-Purcell radiation. *Phys. Rev. ST Accel. Beams* **18**, 052801 (2015).
24. Pendry, J. & Martin-Moreno, L. Energy loss by charged particles in complex media. *Phys. Rev. B* **50**, 5062–5073 (1994).
25. García de Abajo, F. J. Smith-Purcell radiation emission in aligned nanoparticles. *Phys. Rev. E* **61**, 5743–5752 (2000).
26. García de Abajo, F. J. Optical excitations in electron microscopy. *Rev. Mod. Phys.* **82**, 209–275 (2010).
27. Miller, O. D. et al. Fundamental limits to optical response in absorptive systems. *Opt. Express* **24**, 3329–3364 (2016).
28. Yang, Y., Miller, O. D., Christensen, T., Joannopoulos, J. D. & Soljačić, M. Low-loss plasmonic dielectric nanoresonators. *Nano Lett.* **17**, 3238–3245 (2017).
29. Miller, O. D., Johnson, S. G. & Rodriguez, A. W. Shape-independent limits to near-field radiative heat transfer. *Phys. Rev. Lett.* **115**, 204302 (2015).
30. Friedman, A., Gover, A., Kurizki, G., Ruschin, S. & Yariv, A. Spontaneous and stimulated emission from quasifree electrons. *Rev. Mod. Phys.* **60**, 471–535 (1988).
31. Massuda, A. et al. Preprint at https://arxiv.org/abs/1710.05358 (2017).
32. Gradshteyn, I. S. & Ryzhik, I. M. in *Tables of Integrals, Series, and Products* 6th edn (eds Jeffrey, A. & Zwillinger, D.) 843–850 and 1022–1025 (Academic, San Diego, CA, 2000).
33. Pendry, J., Martin-Moreno, L. & Garcia-Vidal, F. Mimicking surface plasmons with structured surfaces. *Science* **305**, 847–848 (2004).
34. Andrews, H. L. & Brau, C. A. Gain of a Smith-Purcell free-electron laser. *Phys. Rev. ST Accel. Beams* **7**, 070701 (2004).
35. Kumar, V. & Kim, K.-J. Analysis of Smith-Purcell free-electron lasers. *Phys. Rev. E* **73**, 026501 (2006).
36. Green, M. A. Self-consistent optical parameters of intrinsic silicon at 300 K including temperature coefficients. *Sol. Energy Mater. Sol. Cells* **92**, 1305–1310 (2008).
37. Schächter, L. & Ron, A. Smith-Purcell free-electron laser. *Phys. Rev. A* **40**, 876–896 (1989).
38. Peralta, E. A. et al. Demonstration of electron acceleration in a laser-driven dielectric microstructure. *Nature* **503**, 91–94 (2013).
39. Breuer, J. & Hommelhoff, P. Laser-based acceleration of nonrelativistic electrons at a dielectric structure. *Phys. Rev. Lett.* **111**, 134803 (2013).
40. Palik, E. D. *Handbook of Optical Constants of Solids* Vol. 3 (Academic, San Diego, CA, 1998).

Author contributions

Y.Y., O.D.M., I.K. and M.S. conceived the project. Y.Y. developed the analytical models and numerical calculations. A.M. prepared the sample under study. Y.Y., A.M., C.R.-C., S.E.K. and I.K. performed the experiment. Y.Y., T.C. and O.D.M. analysed the asymptotics and bulk loss of the limit. S.G.J., J.D.J., O.D.M., I.K. and M.S. supervised the project. Y.Y. wrote the manuscript with input from all authors.

Competing interests

The authors declare no competing interests.

Additional information

Supplementary information is available for this paper at https://doi.org/10.1038/s41567-018-0180-2.

Reprints and permissions information is available at www.nature.com/reprints.

Correspondence and requests for materials should be addressed to Y.Y. or O.D.M. or I.K.

Publisher's note: Springer Nature remains neutral with regard to jurisdictional claims in published maps and institutional affiliations.

Methods

Fourier transform convention. Throughout the paper, we adopt the following Fourier transform conventions

$$f(\omega) \triangleq \int f(t)e^{i\omega t}dt, \quad f(t) \triangleq \frac{1}{2\pi}\int f(\omega)e^{-i\omega t}d\omega \qquad (7)$$

$$g(\mathbf{k}) \triangleq \int f(\mathbf{r})e^{-i\mathbf{k}\cdot\mathbf{r}}d\mathbf{r}, \quad g(\mathbf{r}) \triangleq \frac{1}{(2\pi)^3}\int g(\mathbf{k})e^{i\mathbf{k}\cdot\mathbf{r}}d\mathbf{k} \qquad (8)$$

Numerical methods. The photonic band structure in Fig. 4b is calculated via the eigenfrequency calculation in COMSOL Multiphysics. Numerical radiation intensities (Figs. 1d,e, 2b,c, 3d and 4d–f) are obtained via the frequency-domain calculation in the radiofrequency module in COMSOL Multiphysics. A surface (for 3D problems) or line (for 2D problems) integral on the Poynting vector is calculated to extract the radiation intensity at each frequency.

Experimental set-up and sample fabrication. Our experimental set-up comprises a conventional SEM with the sample mounted perpendicular to the stage. A microscope objective was placed on the SEM stage to collect and image the light emission from the surface. The collected light was then sent through a series of free-space optical elements, enabling simultaneous measurement of the spectrum and of the spatial radiation pattern.

The SEM used for the experiment was a JEOL JSM-6010LA. Its energy spread at the gun exit was in the range 1.5 to 2.5 eV for the range of acceleration voltages considered in this paper. The SEM was operated in spot mode, which we controlled precisely to align the beam so that it passes tangentially to the surface near the desired area of the sample. A Nikon TU Plan Fluor 10x objective with a numerical aperture of 0.30 was used to collect light from the area of interest. The monochrome image of the radiation was taken using a Hamamatsu CCD (charge-coupled device). The spectrometer used was an Action SP-2360-2300i with a low-noise Princeton Instruments Pixis 400 CCD.

A 1D grating (Au-covered single-crystalline Si: periodicity, 140 nm; filling factor, 50%; patterned Si thickness, 53 ± 1.5 nm; Au thickness 44 ± 1.5 nm) was used as the sample in our experiment. The original nanopatterned linear silicon stamp was obtained from LightSmyth Technologies and coated using an electron beam evaporator with a 2 nm Ti adhesion layer and 40 nm of Au at 10^{-7} torr. The sample was mounted inside the SEM chamber to enable the alignment of free electrons to pass in close proximity to the stamps. The emitted light was coupled out of the SEM chamber to a spectrometer, while a camera was used to image the surface of the sample.

Data availability. The data that support the plots within this paper and other findings of this study are available from the corresponding author upon reasonable request.